Heat Transfer in Nuclear Waste Glasses: Measurements and Modeling of Thermal Radiation Properties

FERKL, Pavel, MARCIAL, José, RIGBY, Jessica C., GEORGE, Jaime L., ANAND, Khyati, PEZL, Radek, KLOUŽEK, Jaroslav, SCRIMSHIRE, Alex <http://orcid.org/0000-0002-6828-3620>, PROKHORENKO, Oleg A., HRMA, Pavel, KRUGER, Albert A. and POKORNÝ, Richard

---

This document is the Published Version [VoR]

Citation:

FERKL, Pavel, MARCIAL, José, RIGBY, Jessica C., GEORGE, Jaime L., ANAND, Khyati, PEZL, Radek, KLOUŽEK, Jaroslav, SCRIMSHIRE, Alex, PROKHORENKO, Oleg A., HRMA, Pavel, KRUGER, Albert A. and POKORNÝ, Richard (2026). Heat Transfer in Nuclear Waste Glasses: Measurements and Modeling of Thermal Radiation Properties. Journal of the American Ceramic Society, 109 (3): e70647. [Article]

Journal of the American Ceramic Society

RESEARCH ARTICLE OPEN ACCESS

Heat Transfer in Nuclear Waste Glasses: Measurements and Modeling of Thermal Radiation Properties

Pavel Ferkl[1] | José Marcial[1] | Jessica C. Rigby[1] | Jaime L. George[1] | Khyati Anand[1] | Radek Pezl[2] | Jaroslav Kloužek[2,3] | Alex Scrimshire[4] | Oleg A. Prokhorenko[5] | Pavel Hrma[6] | Albert A. Kruger[7] | Richard Pokorný[2,3]

[1]Pacific Northwest National Laboratory, Richland, Washington, USA | [2]University of Chemistry and Technology Prague, Prague 6, Czechia | [3]Institute of Rock Structure and Mechanics of the Czech Academy of Sciences, Prague 8, Czechia | [4]Materials and Engineering Research Institute, College of Business, Technology and Engineering, Sheffield Hallam University, Sheffield, UK | [5]L.G.P. International, LLC, Livonia, Michigan, USA | [6]AttainX, Support Services Contractor to the Hanford Field Office, U.S. Department of Energy, Richland, Washington, USA | [7]U.S. Department of Energy, Hanford Field Office, Richland, Washington, USA

Correspondence: Pavel Ferkl (pavel.ferkl@pnnl.gov)

Received: 10 October 2025 | **Revised:** 22 January 2026 | **Accepted:** 4 March 2026

Keywords: boron-silicate glass | heat transfer by radiation | nuclear waste | radiation thermal conductivity | scattering

ABSTRACT

We measured and modeled near-infrared extinction of nuclear waste glasses from 300°C to 1150°C to enable predictive radiation heat transfer and thermal conductivity estimates. A composition- and redox-informed model resolved contributions from key chromophores (Fe^{+2}-O-Fe^{+3}, V^{+4}, free and bonded ≡Si-OH groups) and, when present, spinel particles that can cause strong scattering. The model reproduced measured absorption from room temperature up to 1150°C, with minor discrepancies near 1 μm (likely due to possible trace impurities) and 2.5 μm (linked to uncertainty in hydroxy groups). Spectra showed silicate melts were semitransparent mainly in the 0.5–4.0 μm window, responsible for radiation thermal conductivity that generally increases with increasing temperature. We quantified the dependence of effective thermal conductivity on dissolved water and provided distributions across >100 LAW/HLW/DFHLW melts at 1150°C, supporting improved melter heat transfer modeling.

1 | Introduction

The long-term, safe disposal of radioactive waste from both legacy nuclear weapons programs and commercial power generation remains a significant global challenge [1–3]. The internationally accepted strategy for immobilizing high-level waste (HLW) and the baseline for low-activity nuclear waste at Hanford is vitrification, a process in which the waste plus additives are vitrified into a durable borosilicate glass matrix [4]. This method effectively locks radionuclides within the glass structure, ensuring long-term stability and minimizing the risk of environmental contamination [5]. At sites like the Hanford Waste Treatment and Immobilization Plant (WTP) in Washington State, USA, this technology is being deployed on an industrial scale to treat millions of liters of legacy waste [6, 7].

The vitrification process is often carried out in large, continuously operated, Joule-heated ceramic melters [8–12]. The operational success of these melters—including their processing rate, energy efficiency, and overall lifespan—is critically dependent on heat transfer phenomena. In modern waste vitrification melters where convection is enhanced by bubblers, convective heat transfer dominates in the bulk of the molten glass pool [13–15]. However, overall performance is often limited by the rate of heat transfer within the thermal boundary layers, specifically at the interface with the reacting batch materials (the "cold cap") and the interface with melter walls and electrodes [16, 17]. In these regions, heat transfer is both conductive and radiative. Thermal radiation dominates over phonon conduction at the operating temperatures (typically around or exceeding 1150°C) when the glass melt is semi-transparent and free of crystals and bubbles.

https://doi.org/10.1111/jace.70647

The radiation properties of the glass are therefore critical as they control the melting rate of the batch and the heat losses to the melter system [18]. In the nuclear waste melters, the effect of thermal conductivity on the melting rate has not been established because of the lack of reliable thermal conductivity data and complex conditions below the cold cap [19–21].

The radiation properties of glass melts are complex and depend on several interconnected factors. The chemical composition of the glass is paramount, as the absorption of thermal radiation in the near-infrared (NIR) spectrum is dominated by the presence of transition metals and other multivalent ions, such as iron, chromium, nickel, manganese, and vanadium [22, 23]. The specific contribution of each element is further complicated by its redox state; for example, the presence of ferrous ion (Fe^{2+}) causes strong absorption of thermal radiation whereas the ferric ion (Fe^{3+}) shows just a long-wavelength tail of its near-UV band in NIR range [24, 25]. Consequently, the redox conditions within the melter, dictated by the reducing and oxidizing potential of batch components and the gas in which the melt is in contact with (bubbles and external atmosphere), significantly influence the overall heat transfer. Furthermore, in order to maximize the fraction of the nuclear waste in the produced glasses, nuclear waste glasses are often formulated to their solubility limits and may contain microscopic inclusions of liquids (molten salts), gases (primary and secondary bubbles), and solids (dissolving refractory particles and precipitated crystalline phases, such as spinel) that attenuate radiation through both absorption and scattering, adding another layer of complexity [26–29].

Knowledge of the effective thermal conductivity, which combines the contributions of conduction and radiation, is therefore critical for simulating and optimizing melter performance through computational fluid dynamics (CFD) models [30]. Yet developing a comprehensive understanding of this property presents significant challenges. Experimental measurements of high-temperature radiative properties are costly and require highly specialized, custom-built spectrophotometers, which are not widely accessible [31–36]. The direct measurement of the effective conductivity is likewise challenging as the sample thickness in steady state methods or the thermal penetration depth in the transient methods has to be kept below approximately 200 μm to suppress the convection [37] and sealed to avoid volatility. At these length scales, the radiation heat transfer becomes complicated as depending on melt composition, the diffusion approximation is no longer valid, and the concept of effective thermal conductivity is no longer applicable. These limitations create a pressing need for robust, validated compositional models that can evaluate the effective thermal conductivity from the glass composition and processing conditions. Although Choudhary and Potter [24] developed a model for calculating absorption coefficients for commercial silicate glasses with varying content of transition metals, their approach has not been tested for nuclear waste glasses, which often contain the transition metals in significantly higher concentrations.

The primary objective of this study was to develop and experimentally validate a comprehensive model that calculates thermal radiation properties and effective thermal conductivity of nuclear waste glasses as a function of their composition, temperature, redox state, and the presence of inclusions. Section 2 details the theoretical framework for modeling redox equilibria, particle size distributions, and radiative properties. Section 3 describes experimental methods to fabricate glass samples and characterize their properties. In Section 4, the model predictions are compared to experimental measurements for a series of waste glass compositions. Finally, Section 5 discusses implications of these findings for major classes of Hanford nuclear waste and the practical operation of vitrification melters.

2 | Theory

2.1 | Redox State

Nuclear waste glasses are multicomponent boron-silicate systems that contain several polyvalent elements such as Fe, Cr, Ni, Mn, V, U, Ce, etc., the oxidation states of which have unique absorption coefficients. The oxidation states of elements are affected by the batch makeup, by the thermal history during melting and cooling of the glass, and by the composition of the atmosphere under which the glass is processed.

Following the work of Schreiber et al. [38, 39], the local equilibrium between a metallic oxide and oxygen is a function of temperature, T, and the oxygen partial pressure, p_{O_2}. The equilibrium concentration ratio between two specific redox states of a polyvalent element can be calculated as [25]

$$\ln\left(\frac{w_{\mathrm{red}}}{w_{\mathrm{ox}}}\right) = \alpha - \frac{\sigma}{4}\ln\left(p_{O_2}\right) - \frac{\Delta H}{RT} \qquad (1)$$

where w_{red} and w_{ox} are the mass fractions of reduced and oxidized states, respectively, R is the universal gas constant ($8.314\ \mathrm{J\ mol^{-1}K^{-1}}$), σ is the number of electrons separating the reduced and oxidized state, and ΔH is the reaction enthalpy, and α is related to reaction entropy and activity coefficients of oxygen and the ions [25]. Values of σ, α, and ΔH are listed in Table 1 for major redox pairs occurring in nuclear waste glasses. The effect of Fe_2O_3 concentration on parameters α and ΔH was investigated in Savannah River 131 frit [25, 38, 39] but for lack of available data for other elements, we neglected the parameter dependence on glass composition. For elements not listed, we assume that they are present in a predominant oxidation state (see Table 2 for a full list of components).

During high-temperature measurements under air atmosphere, glass melt gradually changes redox state as it equilibrates with air through oxygen diffusion. Thus, sample analysis performed at elevated temperatures (measurement of extinction spectra measurements and oxygen partial pressure) were designed to minimize this effect by limiting the time the samples spent at high temperatures as much as practically possible.

2.2 | Particle Analysis

To maximize the content of waste in nuclear waste glasses, the glasses are permitted to contain a small amount of crystalline particles such as spinel, eskolaite, baddeleyite, nosean, or various phosphate or other phases [28, 40, 41] as long as the resulting

TABLE 1 | Redox model parameters collected from literature [25, 38, 39].

Reaction	$\sigma(\ln(\mathrm{Pa})^{-1})$	α	ΔH (kJ mol^{-1})
Mn^{+3}/Mn^{+2}	1	9.49	55.6
Ce^{+4}/Ce^{+3}	1	6.59	46.0
Cr^{+6}/Cr^{+3}	3	11.37	41.8
Cu^{+2}/Cu^{+1}	1	16.01	175.7
U^{+6}/U^{+5}	1	14.03	171.5
V^{+5}/V^{+4}	1	12.93	171.5
Fe^{+3}/Fe^{+2}	1	12.60	172.0
Cr^{+3}/Cr^{+2}	1	15.33	242.7
V^{+4}/V^{+3}	1	6.62	154.8
Eu^{+3}/Eu^{+2}	1	7.32	171.5
Ti^{+4}/Ti^{+3}	1	3.52	146.4
Ni^{+2}/Ni^{+0}	2	22.52	343.1
Fe^{+2}/Fe^{+0}	2	18.72	334.7
S^{+6}/S^{-2}	8	46.27	786.6

TABLE 2 | Target composition of glass samples in mass%.

	LAWC100	LAWA44	APPS-09	Al-19_MF
Al_2O_3	10.35	6.10	10.55	24.01
B_2O_3	13.94	8.84	4.01	19.22
Bi_2O_3	0.00	0.00	0.00	1.14
CaO	8.17	1.96	10.00	5.59
Cl	0.00	1.17	0.13	0.00
Cr_2O_3	0.02	0.02	0.03	0.52
Cs_2O	0.00	0.15	0.00	0.00
F	0.19	0.00	1.53	0.67
Fe_2O_3	1.02	6.87	0.62	5.91
K_2O	0.15	0.44	0.00	0.14
Li_2O	0.00	0.00	4.51	3.58
MgO	1.02	1.96	0.00	0.12
MnO	0.00	0.00	0.04	0.00
Na_2O	20.38	20.66	13.32	9.60
NiO	0.03	0.00	0.00	0.40
P_2O_5	0.28	0.00	0.30	1.05
PbO	0.01	0.00	0.00	0.41
SiO_2	37.31	43.83	49.51	27.05
SO_3	0.00	0.19	1.45	0.20
TiO_2	0.00	1.96	0.00	0.00
V_2O_5	1.02	0.00	4.07	0.00
ZnO	3.06	2.92	0.00	0.00
ZrO_2	3.06	2.94	0.00	0.39

waste form is durable [42, 43] and particle settling does not disrupt the melter operation [13, 44–46].

A Python code was developed to quantify the number of particles, N_{p}, and their areas, A_{p}, in scanning electron microscope (SEM) images of glass samples using *scikit-image* package [47]. The script implements several steps—Gaussian filtering to reduce noise, Otsu's thresholding method [48] for particle segmentation, filling of small holes and removal of small objects for additional image cleaning, and labeling and measurement of individual particles. As the particles analyzed in this work were approximately equiaxed, they were characterized using an apparent equivalent particle diameter defined as

$$d_{\mathrm{app}} = \sqrt{\frac{4A_{\mathrm{p}}}{\pi}} \tag{2}$$

Since d_{app} determined from cross-section images generally does not correspond to the real 3D particle diameter, d, as they essentially measure slices of the embedded particles, we used the Saltykov method [49] implemented by the *GrainSizeTools* package [50] to infer the probability density function of the 3D particle size distribution, f, from the 2D distribution of d_{app}. The total number of particles per unit volume, N_{total}, is as follows:

$$N_{\mathrm{total}} = \frac{V_V}{\int_0^{\infty} f \frac{\pi d^3}{6} \mathrm{d}d} \tag{3}$$

where V_V is the volume fraction of particles, assumed to be equal to the area fraction of particles, A_A. Finally, the number density distribution of equivalent 3D particle diameters, ρ_{N}, is

$$\rho_{\mathrm{N}} = N_{\mathrm{total}}\, f \tag{4}$$

2.3 | Radiation Properties

The extinction coefficient, β, which accounts for both absorption and scattering, represents the attenuation of thermal radiation in semitransparent media; it is a function of temperature and wavelength. For glass processing, β can be neglected for wavelengths below 0.5 µm, as high-energy photons are emitted by the glasses only at much higher temperatures (above ~1450°C). Thus, heat is transferred almost entirely at longer wavelengths. Because of the absorption of the basic silica network, silicate glasses can be treated as opaque above 4-µm wavelength [24]. Thus, we are confined to 0.5–4.0 µm wavelength range. For nuclear waste glasses, β can be expressed as

$$\beta = \kappa_{\mathrm{g}} + \beta_{\mathrm{p}} \tag{5}$$

where κ_{g} and β_{p} account for the radiation absorption of the glass matrix and the extinction by the particles embedded in the glass matrix.

2.3.1 | Glass Matrix Absorption Coefficient

The glass matrix absorption coefficient is given by the relationship:

$$\kappa_{\mathrm{g}} = \ln(10) \sum_i \xi_i w_i \tag{6}$$

where w_i is the ith species mass fraction and ξ_i is the ith species absorptivity per oxide mass fraction in glass. Equation (6) is, strictly speaking, not applicable for high w_i values but still provides a good approximation for glass technology applications. Note that ξ_i is a function of wavelength and temperature and w_i depends on melting temperature, p_{O_2}, and glass composition.

The absorptivity spectra (dependence of ξ_i on wavelength) for transition metals ions and hydroxy groups ranging from room temperature to 1400°C were reported by Volf [51] and Choudhary and Potter [24]. In this work, we obtained ξ_i values for any temperature by interpolation from the two nearest available spectra. Note that in Equation (6), w_i is the mass fraction of the absorbing species, which accounts, by Equation (1), for the disproportionation of the polyvalent species into several oxidation states; here, we consider the following ions; V^{+4}, Cr^{+3}, Cr^{+6}, Mn^{+2}, Mn^{+3}, Fe^{+2}, Fe^{+3}, Co^{+2}, Cu^{+2}, Ni^{+2}, Nd^{+3}, and OH^{-1}.

2.3.2 | Particle Extinction Coefficient

Microscopic gaseous, liquid, or solid inclusions, emerging from batch and/or generated from the melt, scatter and absorb thermal radiation. Since we are dealing with particles of sizes comparable with the wavelength of the thermal radiation, the particle extinction coefficient β_{p} is expressed by Mie theory [52, 53]:

$$\beta_{\mathrm{p}} = \int_0^\infty \rho_{\mathrm{N}} Q_{\mathrm{ext}} \frac{\pi d^2}{4} \mathrm{d}d \tag{7}$$

where ρ_{N} is the particle number density—the distribution of diameters is determined by methods outlined in Section 2.2—and Q_{ext} is the extinction efficiency calculated using the *miepython* package [54]. The value of Q_{ext} depends on the wavelength, λ, the particle size, d, the complex refractive index of the particles, m, and the refractive index of the surrounding glass matrix, n, the value of which is approximated as [24]

$$n = 1.5 - 0.04 \frac{T - 298}{1673 - 298} - 0.07 \frac{\lambda - 0.59}{4.09 - 0.59} \tag{8}$$

where T is in K and λ is in μm. Mie theory is based on independent scattering approximation that assumes the near-field interactions are negligible. The validity of Mie theory depends on the particle size, refractive index, glass matrix absorption, and particle spacing, so no universal volume-fraction limit applies [55–57], but other studies suggest that it is around 1 vol% [58].

2.4 | Thermal Conductivity

In mathematical models of glass-melting furnaces, the thermal conductivity of the glass melt is crucial for computing temperature and velocity fields, heat transfer to the batch, and heat losses through the walls. The composition and temperature dependence of glass melt phonon conductivity, k_{c}, can be estimated using a model by Choudhary and Potter [24]. The two most employed methods for estimating the radiation thermal conductivity, k_{r}, are the discrete ordinate method (DOM) and diffusion (sometimes referred to as Rosseland) approximation (DA) [18]. DOM is a more rigorous method that directly resolves radiation inside the melt, and can be used for ultra-clear melts [18]. Its disadvantage is the increased computational demand over the DA, which converges to the same solution for more absorbing melts [14, 18, 30]. Using DA, k_{r} can be estimated as

$$k_{\mathrm{r}} = \frac{16\sigma T^3}{3\beta_{\mathrm{R}}} \tag{9}$$

where σ is the Stefan-Boltzmann constant (5.67×10^{-8} W m^{-2} K^{-4}) and β_{R} is the Rosseland mean extinction coefficient defined as [59]

$$\frac{1}{\beta_{\mathrm{R}}} = \int_0^\infty \frac{1}{\beta} \frac{\mathrm{d}E_{\mathrm{b}\lambda}}{\mathrm{d}E_{\mathrm{b}}} \mathrm{d}\lambda = \frac{C_1 C_2}{4\sigma T^5} \int_0^\infty \frac{n^2}{\beta \lambda^6} \frac{\mathrm{e}^{C_2/\lambda T}}{\left(\mathrm{e}^{C_2/\lambda T} - 1\right)^2} \mathrm{d}\lambda \tag{10}$$

where $E_{\mathrm{b}\lambda}$ is the emission power given by Planck's law, E_{b} is the total emission power over all wavelengths, and $C_1 = 3.7418 \times 10^{-16}$ W m^2 and $C_2 = 0.014388$ K m are radiation constants. In this case, the combined phonon conduction and radiation is accounted for in the effective conductivity:

$$k_{\mathrm{eff}} = k_{\mathrm{c}} + k_{\mathrm{r}} \tag{11}$$

3 | Experimental

3.1 | Sample Preparation

Table 2 shows compositions of four nuclear waste glasses selected for analysis to display a wide range of major component fractions and estimated radiation properties. A duplicate LAWC100 glass, in which iron oxide was replaced with stoichiometric equivalent of iron oxalate in batch formulation was melted under a reducing N_2 atmosphere (labeled with the "_R" suffix) and Al-19 glass was prepared from a slurry melter feed (labeled with "_MF" suffix).

Samples LAWC100_R, LAWC100, LAWA44, and APPS-09 were prepared by mixing the chemicals listed in Table S1 in an agate mill for 4 min prior to melting. The Al-19_MF and APPS-09_MF melter feeds were prepared by adding the chemicals and minerals listed in Table S2 to deionized water while stirring such that 500 mL of final slurry probes were prepared. All the slurry probes were then dried at 105°C overnight and afterwards carefully crushed and milled to powder in such a fashion as to break up aggregates but minimized effect on the particle size of minerals such as quartz. All samples were then heated to 1150°C, held at 1150°C for 1 h, air-quenched, heated to 1150°C for the second time, held at 1150°C for 1 h again, cast into blocks with approximate dimensions of 10 × 5 × 1.2 cm, annealed at 500°C for 1 h, and furnace cooled. The sample LAWC100_R was melted at 1150°C using a nitrogen atmosphere.

Bulk compositional analysis was performed using a JEOL 8530F electron probe microanalyzer (EPMA) with the operating conditions of 15 kV accelerating voltage, 20 nA probe current, and 50 µm defocused beam. Pieces of glass of ~1 × 1 × 1 mm were mounted into an aluminum sample holder using epoxy resin. The samples were polished down to a 1 µm surface finish and sputtered coated with 2 nm Ir conductive coating. The agreement with the target composition was very good for most components, including radiation-absorbing constituents such as Fe_2O_3 and V_2O_5 (see Figure S1). A notable exception was the measured content of Cr_2O_3 that was slightly higher than the target in three samples and slightly below the target in Al-19_MF. Since the Cr_2O_3 content was low in all-but-one samples, these small deviations should not significantly affect the radiative properties.

3.2 | Redox state

To evaluate the glass redox state, high-temperature in-situ measurements of oxygen partial pressure were performed using the Rapidox system, while the iron redox state in the produced glasses was analyzed using Mössbauer spectroscopy and X-ray Absorption Near Edge Structure (XANES).

GS Rapidox II oxygen analyzer (Glass Service, Czech Republic) is based on the electrochemical measurement of the equilibrium voltage between a reference electrode and a measuring electrode. The measuring electrode consists of an iridium wire, while the reference electrode is immersed in a Ni/NiO mixture, which provides a well-defined oxygen partial pressure. The measured electromotive force (E, in volts) is then used to calculate the oxygen partial pressure via the Nernst equation. Measurements were conducted at temperatures ranging from 1000°C to 1150°C using 10 K/min heating rate, in 50°C increments.

Room temperature ^{57}Fe Mössbauer Spectroscopy was performed on samples with >1 wt% Fe_2O_3 (LAWA44 and Al-19_MF) using the decay of a 25 mCi ^{57}Co source in a Rh matrix to produce 14.4 keV γ-rays to be absorbed by the sample. The source oscillated at a constant acceleration by a SeeCo W304 drive unit, and the γ-rays were detected by a SeeCo 45431 Kr proportional counter operating with 1.630 kV bias voltage applied to the cathode. Spectra of the photons transmitted through the sample were collected over the velocity range of ±6 mm s^{-1} and were calibrated relative to α-Fe [60]. Recoil software was used to fit pseudo-Voight doublets to the collected spectra, and the iron redox state was determined by the ratio of the peak areas of Fe^{3+} and Fe^{2+} sites, assuming a recoil-free fraction ratio of $f(Fe^{3+}/Fe^{2+}) = 1.0$ [61].

XANES measurement was performed on the 6 powdered glass samples at beamline 4-3 at the Stanford Synchrotron Radiation Light source. The beamline was equipped with a Lytle detector for fluorescence measurements to collect absorption spectra at the Fe K-edge and Cr K-edge for the samples and reference materials FeO (Fe^{2+}), Fe_2O_3 (Fe^{3+}), and Fe_3O_4 ($Fe^{2+/3+}$), and Cr_2O_3 (Cr^{3+}) and Na_2CrO_4 (Cr^{6+}). Spectra were collected from 100 eV below to 200 eV above the absorption edge, with an edge step of 0.2 eV over the pre-edge feature. Repeat measurements were taken for each sample. To improve signal to noise, the repeats were averaged and then the spectra normalized. For the Cr K-edge, the pre-edge was fitted by a linear combination fit of the reference materials to determine the average chromium oxidation state. For evaluation of the form of Fe, the pre-edge peak was deconvoluted and the peak energy and amplitude of the constituent peaks were compared with reference materials and assessed using a variogram to determine the oxidation state [62].

3.3 | Particle Analysis

The samples were sectioned and imaged using a JEOL 7001F SEM to ensure they were free of bubbles and particles. The SEM was operated at 15 kV accelerating voltage and 13 nA probe current to analyze the polished sections prepared as described in Section 3.1. In cases where particles were found, their chemical composition was further analyzed using energy dispersive X-ray spectroscopy (EDS) mapping with an Oxford Ultim Max detector (area = 100 mm^2) and processed using Aztec software.

3.4 | Radiation Properties

The radiation properties were characterized by a custom built high-temperature spectrophotometer [31, 32]. It measured the test specimen thickness dependent optical density caused by absorption by all chromophores plus scattering by particles having sizes within wavelength range plus single and multiple reflection from the glass surfaces using a single narrow monochromatic beam from a quartz halogen lamp. The radiation attenuation caused by reflection on holding cell-sample interface was accounted for by determining the cell constant for each sample, which allowed to transform the measured optical density to absorption coefficient, which is free of losses by reflection [32]. Optical and electronic elements were sufficiently distant from the high-temperature furnace to ensure their thermal stability. The samples were analyzed in the spectral range from 0.7 to 3.8 µm and the temperature range from 300°C to 1150°C with the heating rate of 5 K min^{-1} while in the solid state (up to approximately to glass transition temperature, about 500°C) and 10 K min^{-1} in the molten state. Individual spectral scans were completed within 60 s using custom made high-speed monochromators.

4 | Results

4.1 | Redox State

Table 3 lists the oxygen partial pressures determined by Rapidox method at 1150°C and Fe^{2+}/Fe_{tot}, V^{4+}/V_{tot} and Cr^{3+}/Cr_{tot} values obtained from Equation (1) as well as Fe^{2+}/Fe_{tot} and Cr^{3+}/Cr_{tot} values determined by XANES and p_{O_2} values calculated from Fe redox using Equation (1). Compared to the Rapidox method, XANES Fe redox data indicate slightly more reduced conditions in LAWC100, APPS-09, and APPS-09_MF samples, but still within the experimental uncertainty. The XANES Cr redox data suggest more reduced conditions in most of the samples, but the fits were not as good as with the Fe redox (see Figure S2 and Figure S3). This was mostly caused by the weak 1s – 4s transition characteristic for Cr^{3+} in glass samples. Thus, samples without detectable 1s – 3d transition characteristic for Cr^{6+} were determined as containing predominantly Cr^{3+} [63, 64]. The overall trends between the XANES and Rapidox

TABLE 3 | The values of p_{O_2} and Fe^{2+}/Fe_{tot} and Cr^{3+}/Cr_{tot} determined using Rapidox and XANES. For comparison, estimated vales of p_{O_2}, Fe^{2+}/Fe_{tot}, V^{4+}/V_{tot}, and Cr^{3+}/Cr_{tot} are also provided.

	Rapidox				XANES		
Sample	**p_{O_2} (Pa)**	**Fe^{2+}/Fe_{tot}**	**V^{4+}/V_{tot}**	**Cr^{3+}/Cr_{tot}**	**Fe^{2+}/Fe_{tot}**	**Cr^{3+}/Cr_{tot}**	**p_{O_2} (Pa)**
LAWC100_R	2.6×10^{-3}	0.422	0.476	0.98	0.49 ± 0.02	1	5.1×10^{-4}
LAWC100	8.9×10^{2}	0.029	0.037	0.94	0.10 ± 0.16	1	2.8×10^{0}
LAWA44	2.9×10^{4}	0.013	—	0.53	0.00 ± 0.07	1	1.0×10^{5}
APPS-09	9.5×10^{2}	0.029	0.036	0.94	0.04 ± 0.20	1	1.4×10^{2}
APPS-09_MF	1.0×10^{5}	0.009	0.011	0.30	0.06 ± 0.23	1	2.6×10^{1}
Al-19_MF	1.0×10^{5}	0.009	—	0.31	0.00 ± 0.07	0.78 ± 0.08	1.0×10^{5}

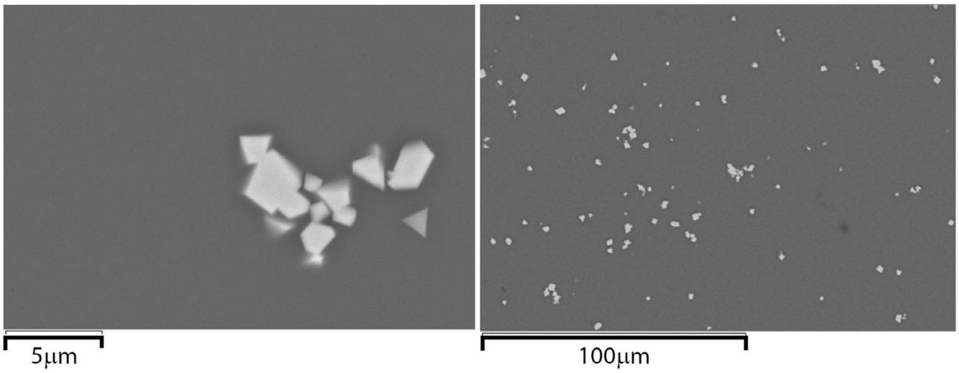

FIGURE 1 | SEM images of spinel crystals in Al-19_MF glass sample.

methods are the same. Reducing atmosphere decreased p_{O_2} below the atmospheric pressure (0.21 bar) and melter feeds (containing nitrates and nitrites) produced more oxidized glasses than oxides precursors. We could not determine vanadium redox directly, thus only V^{4+}/V_{tot} values estimated by Equation (1) are available.

Initial Mössbauer spectroscopy analysis of the reduced iron content was inconclusive because of the low Fe_2O_3 content in four of the samples (see Table 2) and relatively oxidized nature of the other two samples (LAWA44 and Al-19_MF).

We opted to use the Rapidox data for further analysis and discuss potential implications in Section 5.1.

4.2 | Particle Analysis

All melted glasses were found to be clear of bubbles and undissolved batch components by optical microscopy and SEM analysis. Five samples were fully amorphous. Glass Al-19_MF contained ~1 μm particles, some of which clustered into aggregates (see Figure 1). SEM-EDS analysis revealed that the particles were Fe, Cr, Ni, and Mg rich spinel particles (See Figure S4). The presence of spinel particles in HLW glasses is relatively common and has been extensively studied [26, 27, 40, 46, 65–73]. The complex refractive index of the spinel particles was not measured but was approximated by refractive index of magnetite $m = 3.2 + 1.2i$ [74].

TABLE 4 | Average sizes, volume fraction, and number density of spinel crystals in Al-19_MF sample.

Parameter	**Value**
d_{app} (μm)	1.69
d (μm)	1.87
V_V	0.0072
N_{total} (m^{-3})	1.47×10^{-15}

The Al-19_MF sample was sectioned at different locations without detecting significant differences in particle sizes or particle volume fraction. In total, 10 SEM images were analyzed as described in Section 2.2 and illustrated in Figure S5. The averaged results summarized in Table 4 and Figure 2 were used to estimate particle extinction coefficient β_p.

4.3 | Radiation Properties

Absorption spectra were measured from 300°C to 1100°C with 100°C increments, and finally at 1150°C, typical melter operating temperature. Figure 3 shows the results for selected temperatures. Sample Al-19_MF was too opaque to obtain quantitative results. The reduced LAWC100_R sample was the most absorbing, followed by the LAWA44 sample, which had significantly higher iron content compared to the rest of the samples. Compared

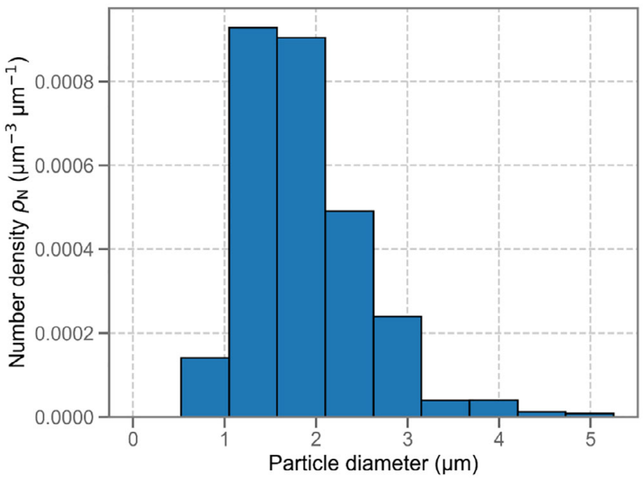

FIGURE 2 | Number density distribution of spinel particles in Al-19_MF sample.

to APPS-09 sample, which was prepared from oxides and carbonates, APPS-09_MF sample, which was prepared from the slurry feed, showed significantly lower absorption around 2.8 μm, attributed to the hydroxy group. The measured effect of temperature on the absorption coefficient was relatively small; the largest effect of increasing temperature was the absorption decrease around 1 μm in LAWC100_R, related to Fe^{2+}, and the increase around 1.5 μm in LAWA44, typical for Cr^{3+} [24].

Figure 4 shows a reasonable agreement between the measured and model estimated absorption coefficients, $\varkappa$, at 1150°C as well as the contributions of individual absorbing species for the most oxidized and the most reduced samples LAWC100_R and APPS-09_MF. Compared to measured data, the model overestimated $\varkappa$ of APPS-09 and underestimated $\varkappa$ of LAWC100 samples. The $\varkappa$ of LAWA44 sample was underestimated at below 2 μm and overestimated above 2 μm. Model estimates were calculated based on target glass composition, measured p_{O_2}, and measured ρ_N. Iron, vanadium, and all (hydroxy) groups in ≡Si-OH were most influential. Chromium and manganese ions were also important for the absorption of Al-19_MF glass matrix, but it was completely overshadowed by at least an order of magnitude higher extinction by the spinel particles. Moreover, the model was able to capture the effect of p_{O_2} on extinction coefficient of LAWC100. The main discrepancies between the measured and modeled are the underestimation of $\varkappa$ around 1 μm wavelength in LAWA44 sample, which could be caused by Cr_2O_3 impurities, and differences in $\varkappa$ around 2.5 μm wavelength in LAWC100 and APPS-09_MF samples, which are likely connected to the content of hydroxy groups. In this work, the content of ≡Si-OH content was not directly measured; by Choudhary and Potter [24], it can be estimated at 0.03 wt%. However, as shown in Section 5.2, the thermal conductivity is not very sensitive to hydroxy group content and thus to absorption coefficient above 2.5 μm.

Figure 5 shows the calculated Rosseland extinction coefficient, β_R, Equation (10), as a function of temperature based on glass composition (and analysis of p_{O_2} and ρ_N) and measured NIR spectra. Silicate glass melts are generally semitransparent for the thermal radiation within the so-called range of transparency between 0.5 and 4 μm. As most of the thermal radiation is emitted above this window at low temperatures, their β_R generally decreases with increasing temperature. The calculated β_R from glass composition displays a comparable agreement with measured spectra from low to high temperatures. The largest discrepancy is found in sample LAWA44, in which β_R is overestimated at low temperatures and underestimated at high temperatures. As this sample contains negligible amounts of Cr_2O_3 and V_2O_5, its absorption is mostly determined by Fe^{2+} and Fe^{3+} content. Similarly, the discrepancies in LAWC100 and APPS-09 samples are linked to V^{4+} content as the most absorbing component in those samples. The sensitivity to the redox state determination is discussed further in Section 5.1.

4.4 | Thermal Conductivity

The phonon thermal conductivity is a weak function of glass melt composition and slightly increases with temperature. It is equal to about 1.6 W m^{-1} K^{-1} at 1150°C [24]. On the other hand, the radiation thermal conductivity depends strongly on the composition through the absorption coefficient. As can be seen in Figure 6, for $\beta \ll 10$ cm^{-1}, radiation is more important heat transfer mode, while for $\beta \gg 10$ cm^{-1}, conduction dominates.

By Equation (9), the radiation conductivity, k_{eff}, is proportional to T^3 and β_R^{-1}. Since β_R decreases with temperature (Figure 5), the dependence on temperature is even stronger than T^3. Figure 7 illustrates how significantly the effective conductivity of waste glasses differ depending on temperature. The Hanford waste melters are operated at 1150°C. At this temperature, only the Al-19_MF sample has high enough extinction coefficient to practically suppress radiation heat transfer. In the other samples, the radiation is the dominant heat transfer mode with the estimated k_{eff} reaching up to 30 W m^{-1} K^{-1} in the APPS-09_MF sample. Figure 7 also shows the large effect of the redox state as LAWC100 and LAWC100_R, and APPS-09 and APPS-09_MF pairs practically differed only in their redox.

The differences between k_{eff} estimated from the glass composition and measured p_{O_2} are largely attributable to the errors in the determination of β_R (see Figure 5). The model systematically overestimates β_R and thus underestimates k_{eff} for the APPS-09 sample at all temperatures. The main absorbing species in this sample is V^{4+}. However, the model estimates k_{eff} of the APPS-09_MF sample, which has the same composition, quite well, highlighting the sensitivity to the glass redox. The model estimated value k_{eff} for Al-19_MF sample, in which thermal radiation is mostly suppressed, is 1.73 W m^{-1} K^{-1} at 1150°C.

5 | Discussion

5.1 | Redox State Determination

In this work, p_{O_2} values were determined independently by Rapidox method. Figure 8 shows that these values correspond relatively well to p_{O_2} values determined by fitting the absorption spectra calculated from glass composition to measured NIR spectra and XANES estimates (Table 3). The largest differences are seen at comparatively low p_{O_2} values in APPS-09_MF and LAWC100 determined by XANES, which leads to overestimation

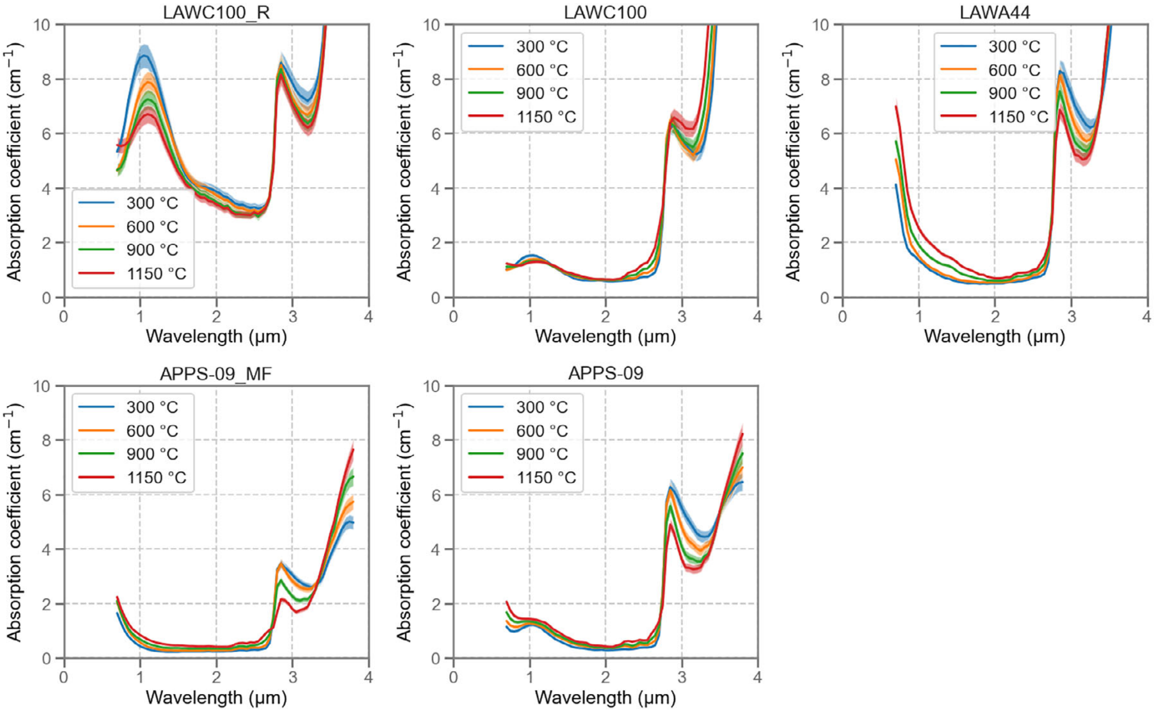

FIGURE 3 | NIR absorption coefficients of waste glasses at several temperatures. The shaded areas represent the estimated uncertainty from multiple measurements.

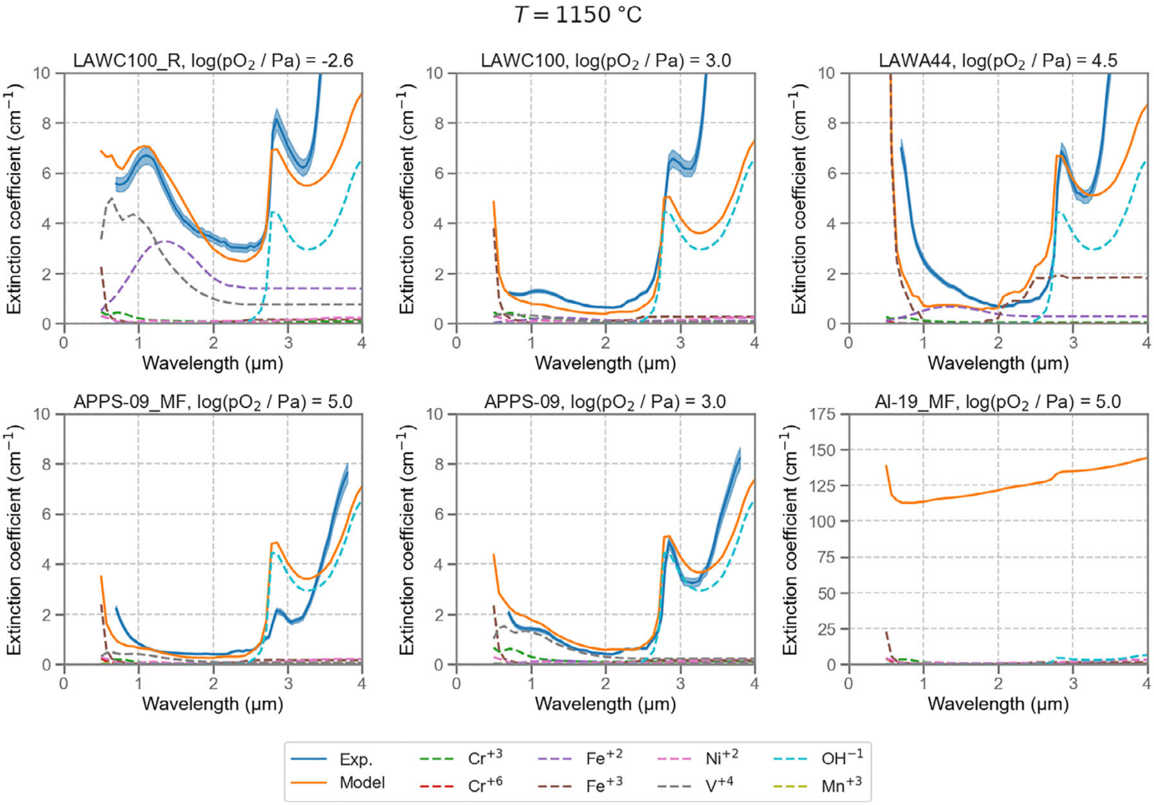

FIGURE 4 | Comparison of measured and modeled NIR extinction coefficients of waste glasses (solid lines). The dashed lines represent the contribution of individual absorbing species. The shaded areas represent the estimated uncertainty from multiple measurements.

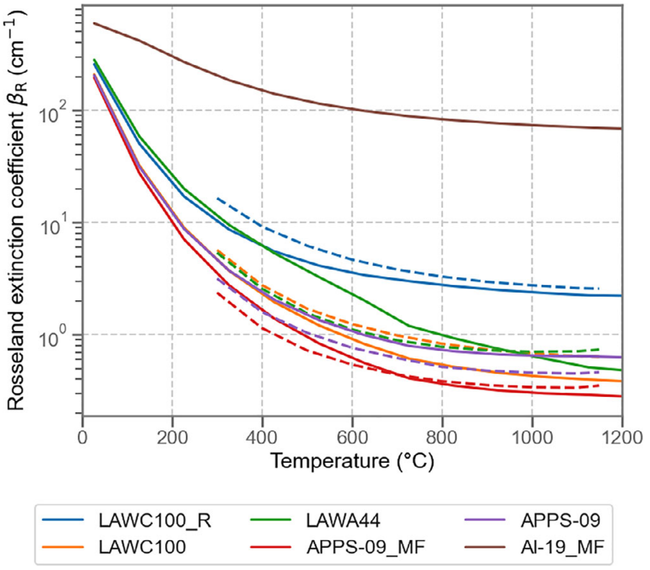

FIGURE 5 | Calculated Rosseland extinction coefficient as a function of temperature based on target composition (solid lines) and measured NIR spectra (dashed lines).

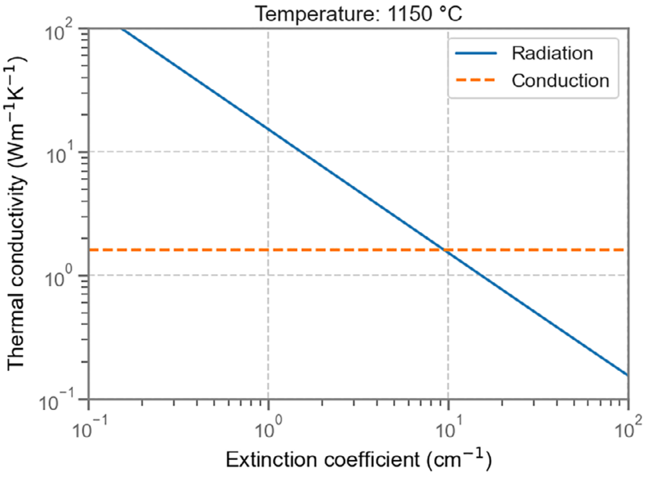

FIGURE 6 | Dependence of phonon and radiation thermal conductivity determined by Rosseland method on the extinction coefficient.

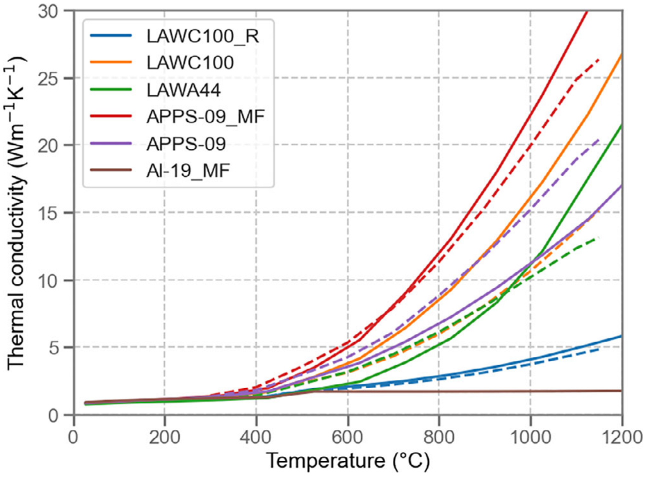

FIGURE 7 | Effective thermal conductivity, Equation (11), as a function of temperature based on model (solid lines) and measured (dashed lines) spectra.

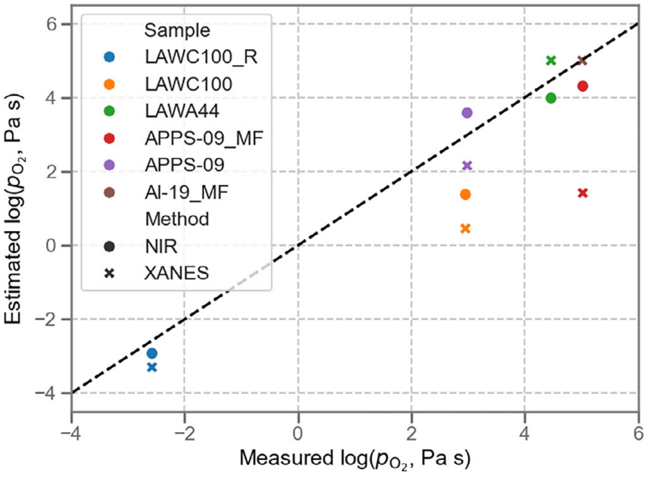

FIGURE 8 | Parity plot between p_{O_2} values measured by the Rapidox method and estimated values determined from iron redox measured by XANES or as best fit to NIR spectra measured at 1150°C.

TABLE 5 | Estimated partial "water" content from the measured spectra.

Sample	$w_{\mathrm{OH}^{-1}}$ (wt%)
LAWC100_R	0.038
LAWC100	0.039
LAWA44	0.031
APPS-09	0.028
APPS-09_MF	0.012

of extinction coefficients in these samples (see Figure 9). It was not possible to obtain the NIR spectrum value for Al-19_MF as the sample was too absorbing.

It can be observed that determining redox directly from the NIR spectra rather then the using an independent measurement yields better agreement with the measured spectra for LAWC100 and APPS-09 samples. The p_{O_2} value alone cannot explain the discrepancies observed in LAWA44 sample. A possible explanation might be that the high iron content either shifts the redox equilibria listed in expressed by parameters in Table 1 or the literature Fe^{2+} and Fe^{3+} absorptivity spectra are no longer valid at these concentrations.

5.2 | Role of Hydroxy Group Content

The content of free hydroxy groups (partial "water" content can be used to compare the glasses of similar system) in the samples was not directly determined but assumed to be equal to 0.03 wt%. The partial "water" content can be determined from the absorption band at 2.87 μm [75]. Table 5 lists the water content obtained by fitting the water content to the measured NIR spectra at 1150°C. Sample APPS-09_MF, which was prepared from the slurry feed, shows significantly lower water content than the rest of the samples. However, it should be noted that the water content is most affected by furnace atmosphere

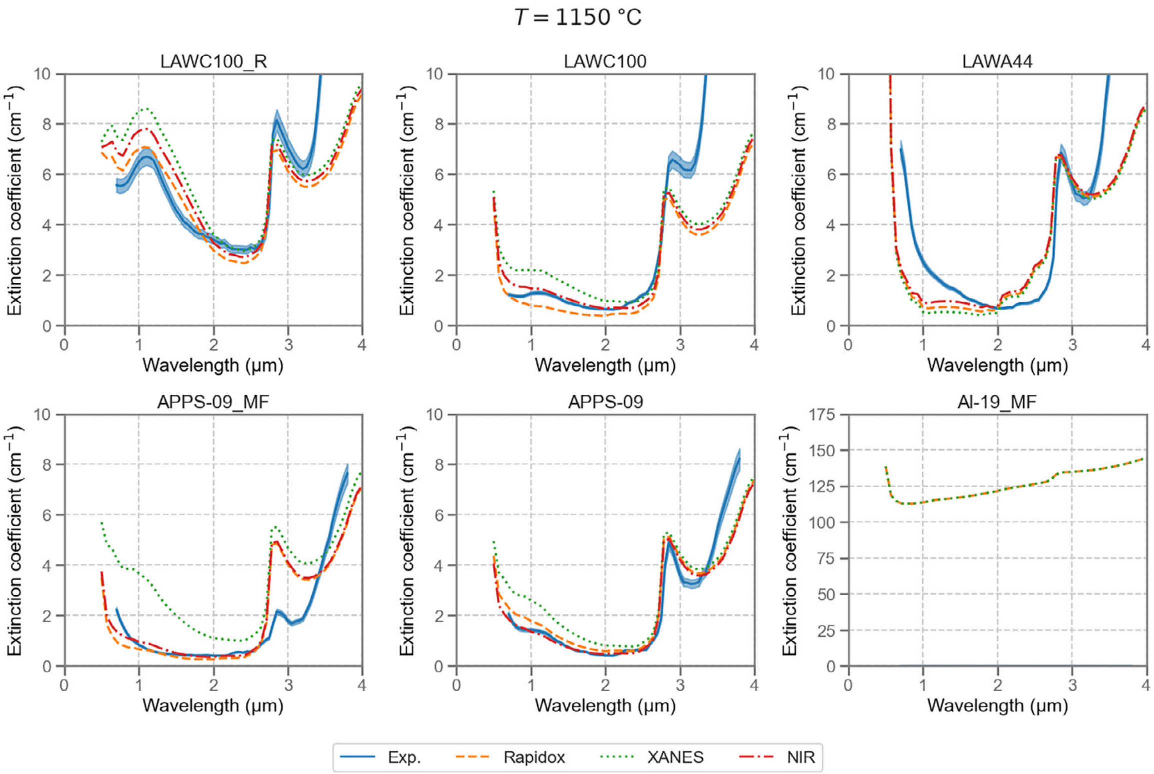

FIGURE 9 | Extinction spectra of investigated waste glasses. Measured data at 1150°C and their uncertainty are shown by solid lines and shaded areas, respectively. Model estimates with p_{O_2} values determined by the Rapidox method, iron redox XANES data, or as best fit to measured NIR spectra are shown with dashed, dotted, and dash-dotted lines, respectively.

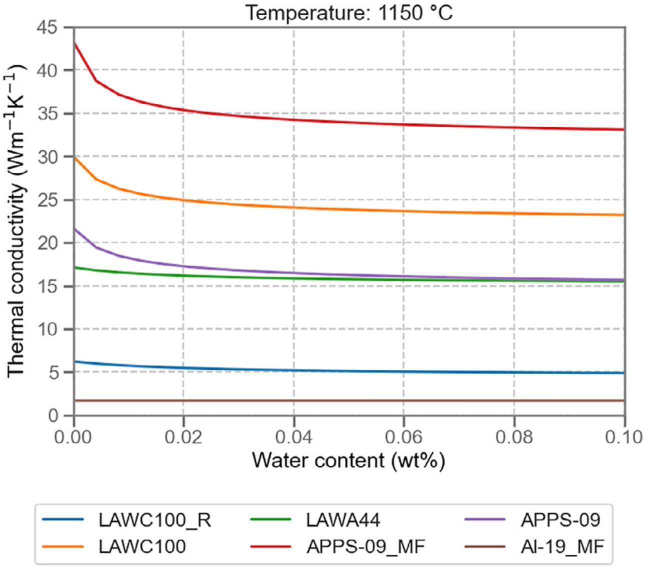

FIGURE 10 | Calculated dependence of effective thermal conductivity on water content.

[76], batch materials, and thermal history, and thus, the water content in our samples may not be representative of glass melts produced in full-scale WTP melters. Figure 10 shows that the effect of the water content on k_{eff} is relatively small for typical water contents, i.e., above 0.03–0.05 wt% in oxygen-gas fired furnaces and on average 0.02 wt% in small-scale electric furnaces [77–79].

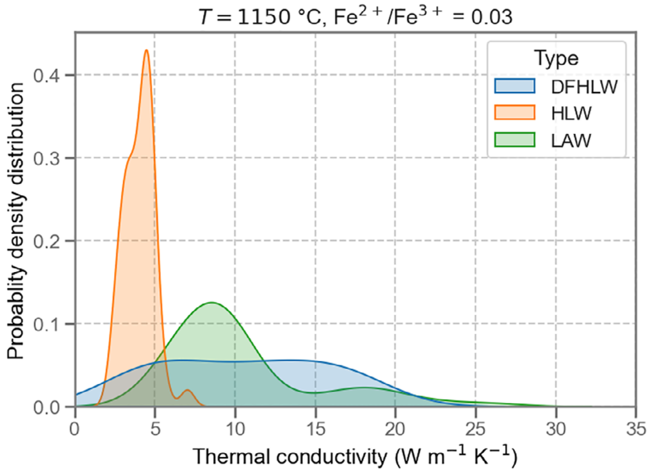

FIGURE 11 | Probability density distribution of effective thermal conductivity at 1150°C and $\mathrm{Fe}^{2+}/\mathrm{Fe}^{3+} = 0.03$ for major classes for nuclear waste glasses.

5.3 | Thermal Conductivity of Different Nuclear Waste Glass Classes

The WTP will process nuclear waste separately as low-activity waste (LAW) (over 90% waste mass) and HLW (over 95% radioactivity) [80, 81]. Figure 11 shows the estimated distribution of effective thermal conductivities, Equation (11), of over 100 glass melts formulated for LAW, HLW, and direct-feed HLW (DFHLW), which accounts for less waste pretreatment [82]. The values were calculated for melt temperature at 1150°C, redox ratio $Fe^{2+}/Fe^{3+} = 0.03$, and assuming no crystals or bubbles. Together with their lower conversion enthalpy [83], the higher effective conductivity of LAW melter feeds contributes to their faster rate of melting, compared to HLW melter feeds.

5.4 | Limitations of Effective Conductivity in Glass Furnace Modeling

Bubbled Joule-heated melters typically maintain a relatively homogeneous glass melt temperature field. In such melters, the effective thermal conductivity of the glass melt primarily affects the heat transfer between the melt and the batch (and thus glass production rate of the melter) and the heat transfer between the melt and the melter walls (and thus thermal efficiency of the melter system). For very clear glass melts, in which DA is no longer applicable [18], the value of the extinction coefficient is also important for modeling the heat transfer between the melt and the melter plenum and the temperature distribution of the melt in the gas-fired furnaces.

5.5 | Role of Inclusions on Heat Transfer Modeling

The glass melt thermal conductivity value is an important parameter of CFD melter models. However, as demonstrated in Figure 7, even relatively small number of particles significantly affects radiation conductivity. In Joule-heated nuclear waste melters, the bottom of the batch (also known as cold cap) consists of primary foam. Small air bubbles can be mixed into the glass melt or nucleated in the melt by redox reactions. Moreover, not all silica and other refractory particles may be fully dissolved in the cold cap and can enter the melt together with spinel and other crystal particles. The quantification of the size and volume fractions of the particles and bubbles near the cold cap and melter walls thus should be a subject of future studies to help guide the heat transfer modeling of vitrification melters. Additionally, self-irradiation of HLW glasses is known to generate defects [84, 85], which will affect the effective thermal conductivity and thus heat transfer during the cooling of waste canisters [86, 87].

6 | Conclusions

We developed a composition- and redox-informed model that predicts NIR extinction using target glass composition, measured oxygen partial pressure, and measured size distribution of inclusions, and validated it against measured spectra from 300°C to 1150°C. The model estimates extinction for multiple HLW/LAW glasses, resolving contributions from Fe, V, OH^-, and other species. From the measured and modeled spectra, we computed the Rosseland extinction and the effective thermal conductivity. Silicate melts are only semitransparent between ~0.5 and 4 μm. In the absence of significant chromium content, the Rosseland extinction generally decreases with increasing temperature, yielding a temperature trend in the radiation component of the effective thermal conductivity that is captured by the model. We provided probability density distributions of effective thermal conductivity at 1150°C for major nuclear waste-glass classes, enabling direct use in melter heat-transfer models; for very clear melts where the diffusion approximation fails, the reported extinction coefficients support modeling of melt–plenum radiation exchange.

Several notable differences between the measured and model estimated absorption spectra have been observed: (i) for LAWA44, extinction around 1 μm is underestimated and the Rosseland-mean extinction is overestimated at low temperature but underpredicted at high temperature; the discrepancy could be caused by high iron content, for which the literature absorptivity spectra are no longer valid, or by error propagation from redox state determination, or the presence of trace Cr_2O_3. (ii) For LAWC100 and APPS-09_MF, discrepancies below ~2.5 μm are likely due to imprecise determination of V^{4+} content and above 2.5 μm because of the hydroxyl content (OH^- estimated at ~0.03 wt%). (iii) In Al-19_MF, absorption by Cr and Mn in the matrix is overwhelmed—by at least an order of magnitude—by extinction from spinel particles.

The work highlights that crystal particles and bubbles originating in the cold cap or from redox reactions measurably increase radiation attenuation, thereby modifying the radiation component of effective thermal conductivity; even in minor fractions. Accurate CFD predictions will therefore benefit from quantifying particle size and shape and bubble size and volume fractions near the cold cap and melter walls. Given the difficulty of high-temperature measurements and the limited applicability of effective-conductivity concepts at small length scales, further work should refine compositional and processing correlations, better constrain inclusion populations, and validate predictions under melter-relevant conditions to reduce uncertainty and improve model predictiveness for design and operation.

Acknowledgments

R. Pezl, J. Klouzek, and R. Pokorny gratefully acknowledge the financial support from the Czech Ministry of Education, Youth and Sports Project No. LUAUS23062. The authors gratefully acknowledge the financial support provided by the U.S. Department of Energy (DOE) Waste Treatment and Immobilization Plant Project. Pacific Northwest National Laboratory is operated by Battelle for the DOE under contract DE-AC05-76RL01830.

Funding

The authors have nothing to report.

References

1. J. D. Vienna, "Nuclear Waste Vitrification in the United States: Recent Developments and Future Options," *International Journal of Applied Glass Science* 1 (2010): 309–321, https://doi.org/10.1111/j.2041-1294.2010.00023.x.

2. S. A. Darda, H. A. Gabbar, V. Damideh, M. Aboughaly, and I. Hassen, "A Comprehensive Review on Radioactive Waste Cycle From Generation to Disposal," *Journal of Radioanalytical and Nuclear Chemistry* 329 (2021): 15–31, https://doi.org/10.1007/s10967-021-07764-2.

3. R. Clayton, J. Kirk, A. Banford, and L. Stamford, "A Review of Radioactive Waste Processing and Disposal From a Life Cycle Environmental Perspective," *Clean Technologies and Environmental Policy* 27 (2025): 665–682, https://doi.org/10.1007/s10098-024-02998-6.

4. J. S. McCloy, B. J. Riley, M. C. Dixon Wilkins, et al., "International Perspectives on Glass Waste Form Development for Low-level and Intermediate-level Radioactive Waste," *Materials Today* 80 (2024): 594–618, https://doi.org/10.1016/j.mattod.2024.08.025.

5. N. R. Council, *Waste Forms Technology and Performance: Final Report* (The National Academies Press, 2011), https://doi.org/doi:10.17226/13100..

6. H. A. Colburn and R. A. Peterson, "A History of Hanford Tank Waste, Implications for Waste Treatment, and Disposal," *Environmental Progress & Sustainable Energy* 40 (2021): e13567, https://doi.org/10.1002/ep.13567.

7. J. K. Bernards, G. A. Hersi, T. M. Hohl, et al., "River Protection Project System Plan. ORP-11242, Rev. 9, US Department of Energy, Office of River Protection," (2020).

8. H. Li, Z. Xing, S. Xu, and S. Liu, "3D Simulation of Borosilicate Glass All-Electric Melting Furnaces," *Journal of the American Ceramic Society* 97 (2014): 141–149, https://doi.org/10.1111/jace.12597.

9. M. Choudhary, "A Three-Dimensional Mathematical Model for Flow and Heat Transfer in Electric Glass Furnaces, 1985 Annual Meeting Industry Applications Society," (1985).

10. G. Suneel, P. M. Satya Sai, C. P. Kaushik, J. K. Gayen, K. V. Ravi, and A. Roy, "Experimental Investigation and Numerical Modeling of a Joule-Heated Ceramic Melter for Vitrification of Radioactive Waste," *Journal of Hazardous, Toxic, and Radioactive Waste* 23 (2019): 04018035, https://doi.org/10.1061/(ASCE)HZ.2153-5515.0000429.

11. C. Giessler and A. Thess, "Numerical Simulation of Electromagnetically Controlled Thermal Convection of Glass Melt in a Crucible," *International Journal of Heat and Mass Transfer* 52 (2009): 3373–3389, https://doi.org/10.1016/j.ijheatmasstransfer.2009.01.004.

12. A. Abbassi and K. Khoshmanesh, "Numerical Simulation and Experimental Analysis of an Industrial Glass Melting Furnace," *Applied Thermal Engineering* 28 (2008): 450–459, https://doi.org/10.1016/j.applthermaleng.2007.05.011.

13. P. Schill, W. Lutze, W. Gong, and I. L. Pegg, "Testing and Modelling the Behaviour of Platinoids During Vitrification of High Level Radioactive Waste. Part 2, Glass Technology," *European Journal of Glass Science and Technology Part A* 48 (2007): 276–289.

14. A. W. Abboud and D. P. Guillen, "A Methodology to Reduce the Computational Cost of Transient Multiphysics Simulations for Waste Vitrification," *Computers & Chemical Engineering* 115 (2018): 64–80, https://doi.org/10.1016/j.compchemeng.2018.03.027.

15. D. P. Guillen, P. Ferkl, R. Pokorny, M. Hall, P. Hrma, and A. A. Kruger, "Numerical Modeling of Joule Heated Ceramic Melter," *Materials Letters* 362 (2024): 136201, https://doi.org/10.1016/j.matlet.2024.136201.

16. A. W. Abboud, D. P. Guillen, P. Hrma, A. A. Kruger, J. Klouzek, and R. Pokorny, "Heat Transfer From Glass Melt to Cold Cap: Computational Fluid Dynamics Study of Cavities beneath Cold Cap," *International Journal of Applied Glass Science* 12 (2021): 233–244, https://doi.org/10.1111/ijag.15863.

17. P. Hrma, R. Pokorny, S. Lee, and A. A. Kruger, "Heat Transfer From Glass Melt to Cold Cap: Melting Rate Correlation Equation," *International Journal of Applied Glass Science* 10 (2019): 143–150, https://doi.org/10.1111/ijag.12666.

18. M. K. Choudhary, B. Purnode, A. M. Lankhorst, and A. F. J. A. Habraken, "Radiative Heat Transfer in Processing of Glass-forming Melts," *International Journal of Applied Glass Science* 9 (2018): 218–234, https://doi.org/10.1111/ijag.12286.

19. S. Lee, D. A. Cutforth, D. Mar, et al., "Melting Rate Correlation With Batch Properties and Melter Operating Conditions During Conversion of Nuclear Waste Melter Feeds to Glasses," *International Journal of Applied Glass Science* 12 (2021): 398–414, https://doi.org/10.1111/ijag.15911.

20. S. Lee, P. Ferkl, R. Pokorny, et al., "Simplified Melting Rate Correlation for Radioactive Waste Vitrification in Electric Furnaces," *Journal of the American Ceramic Society* 103 (2020): 5573–5578, https://doi.org/10.1111/jace.17281.

21. S. M. Lee, P. Hrma, R. Pokorny, et al., "Heat Transfer From Glass Melt to Cold Cap: Effect of Heating Rate," *International Journal of Applied Glass Science* 10 (2019): 401–413, https://doi.org/10.1111/ijag.13104.

22. E. M. A. Khalil, F. H. ElBatal, Y. M. Hamdy, H. M. Zidan, M. S. Aziz, and A. M. Abdelghany, "Infrared Absorption Spectra of Transition Metals-doped Soda Lime Silica Glasses," *Physica B: Condensed Matter* 405 (2010): 1294–1300, https://doi.org/10.1016/j.physb.2009.11.070.

23. N. V. Suzdal, O. A. Prokhorenko, and V. D. Khalilev, "Absorption Spectra of Cobalt-tinted Alkali-borate Glasses," *Glass and Ceramics* 60 (2003): 71–74, https://doi.org/10.1023/a:1024771612918.

24. M. K. Choudhary and R. M. Potter, Heat Transfer in Glass-Forming Melts, in *Properties of Glass-Forming Melts*, ed. D. Pye, I. Joseph, and A. Montenero, (Routledge, 2005), 249–293.

25. P. Hrma, P. Izak, J. D. Vienna, M.-L. Thomas, and G. M. Irwin, "Partial Molar Liquidus Temperatures of Multivalent Elements in Multicomponent Borosilicate Glass," *Physics and Chemistry of Glasses* 43 (2002): 119–127.

26. C. E. Lonergan, K. Akinloye-Brown, J. Rice, et al., "Micron-sized Spinel Crystals in High Level Waste Glass Compositions: Determination of Crystal Size and Crystal Fraction," *Journal of Nuclear Materials* 514 (2019): 196–207, https://doi.org/10.1016/j.jnucmat.2018.11.039.

27. J. Alton, T. J. Plaisted, and P. Hrma, "Dissolution and Growth of Spinel Crystals in a Borosilicate Glass," *Journal of Non-Crystalline Solids* 311 (2002): 24–35, https://doi.org/10.1016/s0022-3093(02)01325-x.

28. J. D. Vienna, "Compositional Models of Glass/Melt Properties and Their Use for Glass Formulation," *Procedia Materials Science* 7 (2014): 148–155, https://doi.org/10.1016/j.mspro.2014.10.020.

29. X. Lu, J. D. Vienna, and J. Du, "Glass Formulation and Composition Optimization With Property Models: A Review," *Journal of the American Ceramic Society* 107 (2023): 1603–1624, https://doi.org/10.1111/jace.19333.

30. M. K. Choudhary, R. Venuturumilli, and M. R. Hyre, "Mathematical Modeling of Flow and Heat Transfer Phenomena in Glass Melting, Delivery, and Forming Processes," *International Journal of Applied Glass Science* 1 (2010): 188–214, https://doi.org/10.1111/j.2041-1294.2010.00018.x.

31. O. A. Prokhorenko, "Radiative Thermal Conductivity of Melts," in *High Temperature Glass Melt Property Database for Process Modeling*, ed. T. P. Seward 111 and T. Vascott (The American Ceramic Society, 2005), 95–115.

32. O. A. Prokhorenko, O. V. Mazurin, M. V. Chistokolova, S. V. Tarakanov, Y. E. Reznik, and I. N. Anfimova, "Problems of Spectrophotometry of Glass-forming Melts: II. A Technique for Measuring the Absorption Spectra of Glasses and Melts in the Red and near-infrared Ranges at Temperatures From 20 to 1500°C," *Glass Physics and Chemistry* 26 (2000): 187–198, https://doi.org/10.1007/bf02735964.

33. A. J. Faber, "Optical Properties and Redox state of Silicate Glass Melts," *Comptes Rendus Chimie* (2002): 705–712, https://doi.org/10.1016/S1631-0748(02)01439-X.

34. A. J. Faber, M. Rongen, A. Lankhorst, and D. D. S. Meneses, "Characterization of High Temperature Optical Spectra of Glass Melts and Modeling of Thermal Radiation Conductivity," *International Journal of Applied Glass Science* 11 (2020): 442–462, https://doi.org/10.1111/ijag.15111.

35. A. J. Faber, D. da Sousa Meneses, and P. A. van Nijnatten, "High Temperature near IR Spectral Absorption of Clear SiO2-based Glasses," *International Journal of Applied Glass Science* 14 (2023): 366–372, https://doi.org/10.1111/ijag.16636.

36. A. J. Faber, M. Rongen, and D. De Sousa Meneses, "High-temperature near-IR Spectral Properties and Thermal Radiation Conductivity of (un)Colored Silicate Glass Melts," *International Journal of Applied Glass Science* 14 (2022): 189–200, https://doi.org/10.1111/ijag.16603.

37. A. Z. Zhao and J. E. Garay, "High Temperature Liquid Thermal Conductivity: A Review of Measurement Techniques, Theoretical Understanding, and Energy Applications," *Progress in Materials Science* 139 (2023): 101180, https://doi.org/10.1016/j.pmatsci.2023.101180.

38. H. D. Schreiber and A. L. Hockman, "Redox Chemistry in Candidate Glasses for Nuclear Waste Immobilization," *Journal of the American Ceramic Society* 70 (1987): 591–594, https://doi.org/10.1111/j.1151-2916.1987.tb05712.x.

39. H. D. Schreiber, C. W. Schreiber, M. W. Riethmiller, and J. S. Downey, "The Effect of Temperature on the Redox Constraints for the Processing of High-Level Nuclear Waste Into a Glass Waste Form," *MRS Proceedings* 176 (1989): 419, https://doi.org/10.1557/PROC-176-419.

40. J. D. Vienna, P. Hrma, J. V. Crum, and M. Mika, "Liquidus Temperature–composition Model for Multi-component Glasses in the Fe, Cr, Ni, and Mn Spinel Primary Phase Field," *Journal of Non-Crystalline Solids* 292 (2001): 1–24, https://doi.org/10.1016/s0022-3093(01)00874-2.

41. P. Hrma, "Crystallization During Processing of Nuclear Waste Glass," *Journal of Non-Crystalline Solids* 356 (2010): 3019–3025, https://doi.org/10.1016/j.jnoncrysol.2010.03.039.

42. H. Li, P. Hrma, J. D. Vienna, M. Qian, Y. Su, and D. E. Smith, "Effects of Al2O3, B2O3, Na2O, and SiO2 on Nepheline Formation in Borosilicate Glasses: Chemical and Physical Correlations," *Journal of Non-Crystalline Solids* 331 (2003): 202–216, https://doi.org/10.1016/j.jnoncrysol.2003.08.082.

43. X. Lu, I. Sargin, and J. D. Vienna, "Predicting Nepheline Precipitation in Waste Glasses Using Ternary Submixture Model and Machine Learning," *Journal of the American Ceramic Society* 104 (2021): 5636–5647, https://doi.org/10.1111/jace.17983.

44. A. Sakai and S. Ishida, "Reflective Reviews on Japanese High-level Waste (HLW) Vitrification—Exploring the Obstacles Encountered in Active Tests at Rokkasho," *Annals of Nuclear Energy* 196 (2024): 110175, https://doi.org/10.1016/j.anucene.2023.110175.

45. J. Matyas, G. Sevigny, and J. Venarsky, *Evaluation of Crystal Accumulation in High Level Waste Glasses With Research-Scale Melter, PNNL-27419* (Pacific Northwest National Laboratory, 2018), https://doi.org/10.2172/1868935.

46. P. Schill, M. Trochta, J. Matyas, L. Nemec, and P. Hrma, "Mathematical Model of Spinel Settling in a Real Waste Glass Melter, Waste Management Symposia," (2001).

47. S. van der Walt, J. L. Schonberger, J. Nunez-Iglesias, et al., "scikit-image: Image Processing in Python," *PeerJ* 2 (2014): e453, https://doi.org/10.7717/peerj.453.

48. N. Otsu, "A Threshold Selection Method From Gray-Level Histograms," *IEEE Transactions on Systems, Man, and Cybernetics* 9 (1979): 62–66, https://doi.org/10.1109/tsmc.1979.4310076.

49. S. A. Saltikov, *The Determination of the Size Distribution of Particles in an Opaque Material From a Measurement of the Size Distribution of Their Sections* (Springer, 1967), https://doi.org/10.1007/978-3-642-88260-9.

50. M. A. Lopez-Sanchez and S. Llana-Fúnez, "An Extension of the Saltykov Method to Quantify 3D Grain Size Distributions in Mylonites," *Journal of Structural Geology* 93 (2016): 149–161, https://doi.org/10.1016/j.jsg.2016.10.008.

51. M. B. Volf, *Chemical approach to glass* (Elsevier, 1984).

52. M. F. Modest, *Radiative Heat Transfer*, Second ed. (Academic Press, 2003).

53. T. Wriedt and M. Theory, "A Review," in *The Mie Theory: Basics and Applications*, ed. W. Hergert and T. Wriedt (Springer, 2012), 53–71, https://doi.org/10.1007/978-3-642-28738-1_2.

54. S. Prahl, miepython: A Python library for Mie scattering calculations (2025), https://github.com/scottprahl/miepython.

55. A. García-Valenzuela, H. Contreras-Tello, J. A. Olivares, and F. L. S. Cuppo, "Insights Into the Dependent-scattering Contributions to the Extinction Coefficient in Highly Scattering Suspensions," *Journal of the Optical Society of America A Optics and Image Science* 30 (2013): 1328, https://doi.org/10.1364/JOSAA.30.001328.

56. R. A. Yalcin, T. Lee, G. N. Kashanchi, et al., "Dependent Scattering in Thick and Concentrated Colloidal Suspensions," *ACS Photonics* 9 (2022): 3318–3332, https://doi.org/10.1021/acsphotonics.2c00664.

57. J. Zhai, S. Zhang, and L. Liu, "Extinction and Independent Scattering Criterion for Clusters of Spherical Particles Embedded in Absorbing Host Media," (2023), https://doi.org/10.3390/photonics10070782.

58. P. Di Ninni, F. Martelli, and G. Zaccanti, "Effect of Dependent Scattering on the Optical Properties of Intralipid Tissue Phantoms," *Biomedical Optics Express* 2 (2011): 2265, https://doi.org/10.1364/boe.2.002265.

59. J. R. Howell, M. P. Mengüç, K. Daun, and R. Siegel, *Thermal Radiation Heat Transfer* (CRC press, 2020), https://doi.org/10.1201/9780429327308.

60. J. E. Page, C. V. Topping, A. Scrimshire, P. A. Bingham, S. J. Blundell, and M. A. Hayward, "Doped Sr_2FeIrO_6—Phase Separation and a Jeff $\neq$ 0 State for Ir5+," *Inorganic Chemistry* 57 (2018): 10303–10311, https://doi.org/10.1021/acs.inorgchem.8b01539.

61. M. Ahmadzadeh, A. Scrimshire, L. Mottram, et al., "Structure of $NaFeSiO_4$, $NaFeSi_2O_6$, and $NaFeSi_3O_8$ Glasses and Glass-ceramics," *American Mineralogist* 105 (2020): 1375–1384, https://doi.org/10.2138/am-2020-7285.

62. M. Wilke, G. M. Partzsch, R. Bernhardt, and D. Lattard, "Determination of the Iron Oxidation state in Basaltic Glasses Using XANES at the K-edge," *Chemical Geology* 220 (2005): 143–161, https://doi.org/10.1016/j.chemgeo.2005.03.004.

63. M. Tromp, J. Moulin, G. Reid, and J. Evans, "Cr K-Edge XANES Spectroscopy: Ligand and Oxidation State Dependence — What Is Oxidation State?," *AIP Conference Proceedings* 882 (2007): 699–701, https://doi.org/10.1063/1.2644637.

64. M. L. Baker, M. W. Mara, J. J. Yan, K. O. Hodgson, B. Hedman, and E. I. Solomon, "K- and L-edge X-ray Absorption Spectroscopy (XAS) and Resonant Inelastic X-ray Scattering (RIXS) Determination of Differential Orbital Covalency (DOC) of Transition Metal Sites," *Coordination Chemistry Reviews* 345 (2017): 182–208, https://doi.org/10.1016/j.ccr.2017.02.004.

65. D. F. Bickford, P. Hrma, and B. W. Bowan, "Control of Radioactive Waste Glass Melters: II, Residence Time and Melt Rate Limitations," *Journal of the American Ceramic Society* 73 (2005): 2903–2915, https://doi.org/10.1111/j.1151-2916.1990.tb06693.x.

66. J. Alton, T. J. Plaisted, and P. Hrma, "Kinetics of Growth of Spinel Crystals in a Borosilicate Glass," *Chemical Engineering Science* 57 (2002): 2503–2509, https://doi.org/10.1016/s0009-2509(02)00121-5.

67. V. Gervasio, S. A. Saslow, J. B. Lang, et al., "Impacts of Cr(III) and Cr(VI) Concentrations on Key High-level Waste Glass Properties," *International Journal of Applied Glass Science* (2025): e16708, https://doi.org/10.1111/ijag.16708.

68. P. Hrma, P. Schill, and L. Nemec, *Settling of Spinel in A High-Level Waste Glass Melter, PNNL-13747* (Pacific Northwest National Laboratory, 2002), https://doi.org/10.2172/791850.

69. C. E. Lonergan, J. Rice, C. Skidmore, M. J. Schweiger, and P. Hrma, "The Effects of Mixing Multi-component HLW Glasses on Spinel Crystal Size," *Journal of Nuclear Materials* 558 (2022): 153318, https://doi.org/10.1016/j.jnucmat.2021.153318.

70. J. Matyáš, V. Gervasio, S. E. Sannoh, and A. A. Kruger, "Predictive Modeling of Crystal Accumulation in High-level Waste Glass Melters Processing Radioactive Waste," *Journal of Nuclear Materials* 495 (2017): 322–331, https://doi.org/10.1016/j.jnucmat.2017.08.034.

71. J. Matyas, J. D. Vienna, and M. J. Schaible, *Development of Crystal-Tolerant High-Level Waste Glasses, PNNL-20072* (Pacific Northwest National Laboratory, 2010), https://doi.org/10.2172/1009766.

72. S. Annamalai, H. Gan, M. Chaudhuri, W. Kot, and I. Pegg, Spinel crystallization in HLW glass melts: Cation exchange systematics and the role of Rh2O3 in Spinel formation, in *Environmental Issues and Waste Management Technologies in the Ceramic and Nuclear Industries IX*, ed. J.

Vienna and D. Spearing (The American Ceramic Society, 2006), 279–288, https://doi.org/10.1002/9781118407004.ch26.

73. J. Matyáš, D. P. Jansik, A. T. Owen, C. A. Rodriguez, J. B. Lang, and A. A. Kruger, "Impact of Particle Agglomeration on Accumulation Rates in the Glass Discharge Riser of HLW Melter," in *Advances in Materials Science for Environmental and Energy Technologies II*, ed. J. Matyáš, T. Ohji, X. Liu, M.P. Paranthaman, R. Devanathan, K. Fox, M. Singh, and W. Wong-Ng, (Wiley, 2013), 59–68, https://doi.org/10.1002/9781118751176.ch6.

74. M. R. Querry, *Optical Constants, CRDC-CR-85034* (University of Missouri, 1985).

75. R. F. Bartholomew, B. L. Butler, H. L. Hoover, and C. K. Wu, "Infrared Spectra of a Water-Containing Glass," *Journal of the American Ceramic Society* 63 (1980): 481–485, https://doi.org/10.1111/j.1151-2916.1980.tb10748.x.

76. P. R. Laimböck, *Foaming of glass melts* (Technische Universiteit Eindhoven, 1998).

77. P. Kiefer, R. Balzer, J. Deubener, et al., "Density, Elastic Constants and Indentation Hardness of Hydrous Soda-lime-silica Glasses," *Journal of Non-Crystalline Solids* 521 (2019): 119480, https://doi.org/10.1016/j.jnoncrysol.2019.119480.

78. R. G. C. Beerkens and J. van der Schaaf, "Gas Release and Foam Formation during Melting and Fining of Glass," *Journal of the American Ceramic Society* 89 (2006): 24–35, https://doi.org/10.1111/j.1551-2916.2005.00691.x.

79. J. Deubener, R. Müller, H. Behrens, and G. Heide, "Water and the Glass Transition Temperature of Silicate Melts," *Journal of Non-Crystalline Solids* 330 (2003): 268–273, https://doi.org/10.1016/S0022-3093(03)00472-1.

80. A. Goel, J. S. McCloy, R. Pokorny, and A. A. Kruger, "Challenges With Vitrification of Hanford High-Level Waste (HLW) to Borosilicate Glass—An Overview," *Journal of Non-Crystalline Solids: X* 4 (2019): 100033, https://doi.org/10.1016/j.nocx.2019.100033.

81. J. Marcial, B. J. Riley, A. A. Kruger, C. E. Lonergan, and J. D. Vienna, "Hanford Low-activity Waste Vitrification: A Review," *Journal of Hazardous Materials* 461 (2024): 132437, https://doi.org/10.1016/j.jhazmat.2023.132437.

82. K. S. Matlack, I. Pegg, I. Joseph, and W. K. Kot, Support for HLW Direct Feed—Phase 2, VSL-15R3440-1, The Catholic University of America (2017), https://doi.org/10.2172/1347547.

83. M. Vernerová, K. Šůsová, M. Kohoutková, et al., "Effect of Glass Forming Additives on Low-Activity Waste Feed Conversion to Glass," *Journal of Nuclear Materials* 593 (2024): 155003, https://doi.org/10.1016/j.jnucmat.2024.155003.

84. M. I. Ojovan and W. E. Lee, "Alkali Ion Exchange in γ-irradiated Glasses," *Journal of Nuclear Materials* 335 (2004): 425–432, https://doi.org/10.1016/j.jnucmat.2004.07.050.

85. G. Möbus, M. Ojovan, S. Cook, J. Tsai, and G. Yang, "Nano-scale Quasi-melting of Alkali-borosilicate Glasses Under Electron Irradiation," *Journal of Nuclear Materials* 396 (2010): 264–271, https://doi.org/10.1016/j.jnucmat.2009.11.020.

86. D. P. Guillen, *Thermal Predictions of the Cooling of Waste Glass Canisters* (American Nuclear Society Winter Meeting, 2014).

87. N. Barth, D. George, F. Bouyer, et al., "An Inverse Method Predicting Thermal Fluxes in Nuclear Waste Glass Canisters During Vitrification and Cooling," *Nuclear Engineering and Design* 364 (2020): 110686, https://doi.org/10.1016/j.nucengdes.2020.110686.

Supporting Information

Additional supporting information can be found online in the Supporting Information section.

Supporting File 1: jace70647-sup-0001-SuppMat.docx.